

Wavefront sensing and adaptive control in phased array of fiber collimators

Svetlana L. Lachinova^{*a,b} and Mikhail A. Vorontsov^c

^aInstitute for Systems Research, University of Maryland, College Park, MD, USA 20742;

^bOptonicus, 711 E Monument Ave., Ste. 101, Dayton, OH, USA 45402

^cSchool of Engineering, University of Dayton, 300 College Park, Dayton, OH, USA 45469

ABSTRACT

A new wavefront control approach for mitigation of atmospheric turbulence-induced wavefront phase aberrations in coherent fiber-array-based laser beam projection systems is introduced and analyzed. This approach is based on integration of wavefront sensing capabilities directly into the fiber-array transmitter aperture. In the coherent fiber array considered, we assume that each fiber collimator (subaperture) of the array is capable of precompensation of local (on-subaperture) wavefront phase tip and tilt aberrations using controllable rapid displacement of the tip of the delivery fiber at the collimating lens focal plane. In the technique proposed, this tip and tilt phase aberration control is based on maximization of the optical power received through the same fiber collimator using the stochastic parallel gradient descent (SPGD) technique. The coordinates of the fiber tip after the local tip and tilt aberrations are mitigated correspond to the coordinates of the focal-spot centroid of the optical wave backscattered off the target. Similar to a conventional Shack-Hartmann wavefront sensor, phase function over the entire fiber-array aperture can then be retrieved using the coordinates obtained. The piston phases that are required for coherent combining (phase locking) of the outgoing beams at the target plane can be further calculated from the reconstructed wavefront phase. Results of analysis and numerical simulations are presented. Performance of adaptive precompensation of phase aberrations in this laser beam projection system type is compared for various system configurations characterized by the number of fiber collimators and atmospheric turbulence conditions. The wavefront control concept presented can be effectively applied for long-range laser beam projection scenarios for which the time delay related with the double-pass laser beam propagation to the target and back is compared or even exceeds the characteristic time of the atmospheric turbulence change – scenarios when conventional target-in-the-loop phase-locking techniques fail.

Keywords: active or adaptive optics, atmospheric optics, wavefront sensing, phase retrieval, laser arrays, laser beam combining, phase locking

1. INTRODUCTION

In the previous studies^{1,2} we analyzed the potential efficiency of a laser beam projection system composed of an adaptive array of fiber collimators (subapertures). This analysis was based on the assumption that there exists an adaptive optics (AO) system that can provide an ideal measurement and a precompensation of local (on-subaperture) phase aberrations originated both in the fiber-based laser beam delivery system, referred to as a multichannel master oscillator power amplifier (MOPA) system, and along the propagation path from the fiber-array transmitter aperture to the target. Note that these two phase aberration types can be compensated using separate control systems.³

In the present paper, we address the issues related to practical implementation of phase aberration precompensation techniques in the fiber-array beam projection systems. Note that in the conventional AO technique, control signals applied to wavefront correctors (typically deformable mirrors) are computed based on the wavefront sensor data. This approach requires sharing of the same optical propagation path for the outgoing and the received waves, with the received wave being redirected to a wavefront sensor by a beam splitter that is located in front of the outgoing beam. In the case of the fiber-array-based beam director, this conventional AO approach would lead to an integration of wavefront sensing and control capabilities into each subaperture of the fiber array. Such integration represents a challenging technical problem, especially for densely-packed fiber-array systems with a large number of subapertures.

* svetlana@optonicus.com; www.optonicus.com

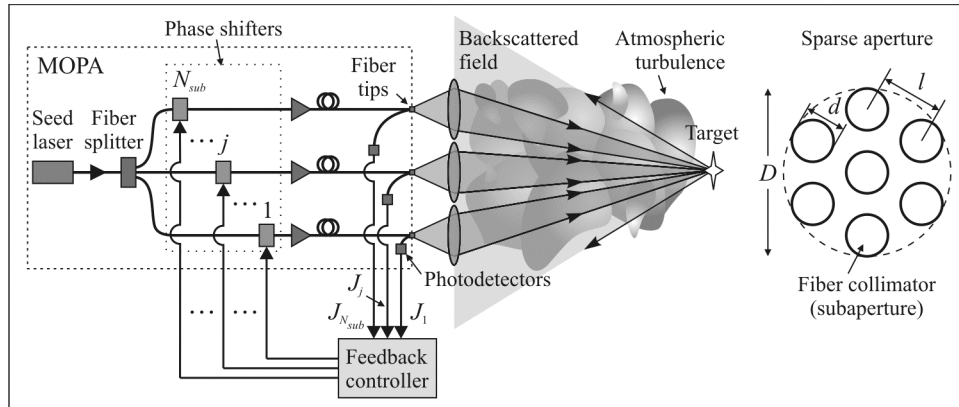


Figure 1. A schematic diagram illustrating wavefront sensing and adaptive control approach for a coherent array of fiber collimators.

In the present study, we show that the wavefront phase aberration sensing in the fiber-array systems can be performed without installation of any additional optical elements that are located inside the optical train of the transmitted laser beams (beamlets) that exit fiber tips of the fiber collimators. To illustrate the idea of the wavefront sensing and adaptive control concept introduced, consider a notional schematic of the fiber-array system shown in Fig. 1 and assume that each fiber collimator of the array is capable of the precompensation of local wavefront phase tip and tilt aberrations using controllable rapid displacement of the fiber tip located in the focal plane of the collimating lens. In order to avoid speckle effects,⁴ restrict our analysis to a laser beam projection onto a remote unresolved (point-source) target. Assume that by controlling the fiber-tip positions, the outgoing beamlets are focused (projected) on the target. The optical wave scattered off the point-source target propagates back to the fiber-array subapertures. Optical inhomogeneities of the propagation medium (atmospheric turbulence) result in phase aberrations as well as in intensity scintillations of the returned optical wave that enters the fiber-array subapertures. The received wavefront is sub-divided by the lens array of the fiber collimators. Similar to a conventional Shack-Hartmann wavefront sensor,⁵⁻⁹ each lens of the fiber collimator array focuses the received optical field onto its focal plane that coincides with the plane of the fiber tip. A portion of the received optical field energy inside each focal spot enters into the core of the single-mode delivery fiber and propagates back to the fiber-coupled photodetector. Separation of the counter-propagating outgoing and received waves in the fiber can be achieved using, for example, directional fiber circulators, free-space fiber isolators, etc. The amount of the received optical power J_j , $j = 1, \dots, N_{sub}$, that enters to the j th photodetector at the j th fiber collimator is inversely proportional to the displacement of the fiber-tip center in respect to a focal-spot centroid position. Here N_{sub} is the number of the fiber collimators in the array. The mismatch between the coordinates of the delivery fiber and the focal-spot centroid is due to the impact of atmospheric-turbulence-induced wavefront tip and tilt aberrations. The received optical wave power at the fiber-collimator array subaperture can therefore be used as a measure (metric) of uncompensated wavefront tip and tilt aberrations. The signals measured by the photodetector at each fiber-array subaperture are referred to as local power-in-the-bucket (PIB) metrics. An optimization of the local PIB metrics using, e.g., the stochastic parallel gradient descent (SPGD)¹⁰⁻¹² or the multi-dithering technique¹³ results in the wavefront tip and tilt aberration precompensation at each subaperture by placing the center of each fiber tip into the location of the corresponding focal-spot centroid. With compensation of the local wavefront tip and tilt aberrations, the centroids of the focal spots can be easily determined from the pre-calibrated dependence of the fiber-tip x and y coordinates on the corresponding control voltages applied to x and y actuators of the fiber-tip positioning system. This allows a retrieval of the atmospheric-turbulence-induced wavefront tip and tilt aberrations at each fiber-array subaperture. Thus, the optimization of the local PIB metrics provides exactly the same information as the conventional Shack-Hartmann sensor with an identical array of lenslets. This information is further used for the recovery of local piston-type phase aberration components, which is required for the precompensation of the turbulence-induced local piston aberrations leading to a coherent combining (phase locking) of the outgoing beamlets at the target plane.

The procedure of the piston phase aberration retrieval used in the present work can be briefly described as follows. The local piston phases are calculated from the wavefront phase that is reconstructed from the tip and tilt aberration data obtained with the fiber-array-based Shack-Hartman (FASH) wavefront sensor described. Among several available techniques for the phase reconstruction based on the Shack-Hartmann sensor, we adopt the so-called modal phase reconstruction algorithm detailed in Ref. [14].

The key advantage of the FASH wavefront sensing approach is that it does not require the wavefront sensing installation of a beam splitter located inside the optical train of the outgoing beamlets. Another important advantage of the wavefront sensing and control concept presented here is that it can be applied for long-range laser beam projection scenarios for which the time delay related with the double-pass laser beam propagation to the target and back is compared or even exceeds the characteristic time of the atmospheric turbulence change – scenarios when conventional target-in-the-loop (TIL) AO techniques fail.^{15,16}

2. PHASED ARRAY OF FIBER COLLIMATORS

2.1 System Architecture and Mathematical Model

Consider a sparse-aperture transceiver telescope of overall diameter D in the form of a hexagonal array of N_{sub} densely-packed circular subapertures of diameter d , as in Fig. 1. For simplicity, we assume that the transmitted beamlets are phase-locked at the system output (pupil) plane $z=0$, i.e., all MOPA-system-induced random phase shifts are compensated using, e.g., the recently developed obscuration-free pupil-plane phase-locking technique.³

In the receiver/sensor mode, the received (backscattered) wave with the complex amplitude $A_{in}(\mathbf{r}, t) = I_{in}^{1/2}(\mathbf{r}, t) \exp[-i\varphi(\mathbf{r}, t)]$ after propagation through the atmospheric turbulence enters a pupil plane. Here $I_{in}(\mathbf{r}, t)$ is the input wave intensity, $\varphi(\mathbf{r}, t)$ is the distorted wavefront phase, $\mathbf{r} = \{x, y\}$ is the radius vector at the pupil plane, and t is the time variable. The complex amplitude of the input optical field at the j th subaperture is therefore given by

$$A_j^{in}(\boldsymbol{\rho}_j, t) = A_j(\boldsymbol{\rho}_j, t) \exp[-i\varphi_j(\boldsymbol{\rho}_j, t)] \quad (j = 1, \dots, N_{sub}), \quad (1)$$

where $\boldsymbol{\rho}_j \equiv \mathbf{r} - \mathbf{r}_j$ is the radius vector with respect to the j th subaperture center \mathbf{r}_j , $A_j(\boldsymbol{\rho}_j, t) = M(\boldsymbol{\rho}_j) I_{in}^{1/2}(\mathbf{r}, t)$ is a positive real function, $\varphi_j(\boldsymbol{\rho}_j, t) = M(\boldsymbol{\rho}_j) \varphi(\mathbf{r}, t)$, and $M(\boldsymbol{\rho}_j)$ is the step-wise window function that equals unity inside the subaperture circular region Ω_j and zero otherwise. The distorted wavefront phase in Eq. (1) is represented in the form

$$\varphi_j(\boldsymbol{\rho}_j, t) = \varphi_j^{at}(\boldsymbol{\rho}_j, t) + \Delta_j^{at}(t), \quad (2)$$

where $\Delta_j^{at}(t)$ and $\varphi_j^{at}(\boldsymbol{\rho}_j, t)$ are the local atmospheric-turbulence-induced pistons and spatially-modulated phase aberrations of the received wave originated from the remote point-source target. Here we assume that the subaperture-averaged phase modulation components $\{\bar{\varphi}_j^{at}(t)\}$ of functions $\{\varphi_j^{at}(\boldsymbol{\rho}_j, t)\}$ equal zero.

In the transmitter mode, the complex amplitude of the outgoing optical field at the j th subaperture $A_j^{out}(\boldsymbol{\rho}_j, t)$ at the output plane $z=0$ can be represented in the following form:

$$A_j^{out}(\boldsymbol{\rho}_j, t) = A_0(\boldsymbol{\rho}_j) \exp[i\phi_j^{out}(\boldsymbol{\rho}_j, t)], \quad (3)$$

where $A_0(\boldsymbol{\rho}_j) = M(\boldsymbol{\rho}_j) I_0^{1/2}(\boldsymbol{\rho}_j)$ and $I_0(\boldsymbol{\rho}_j)$ and $\phi_j^{out}(\boldsymbol{\rho}_j, t)$ are respectively the intensity and the phase of the j th beamlet. We assume that the amplitude $I_0(\boldsymbol{\rho}_j)$ is described by the Gaussian function of radius a_0 for all subapertures, i.e., $I_0(\boldsymbol{\rho}_j) = I_0(0) \exp(-2\rho_j^2/a_0^2)$, where $I_0(0)$ is a constant.

The phase term in Eq. (3) is represented in the form²

$$\phi_j^{out}(\boldsymbol{\rho}_j, t) = u_j^F(\boldsymbol{\rho}_j) + v_j(t) + u_j(\boldsymbol{\rho}_j, t), \quad (4)$$

where $\{u_j^F(\boldsymbol{\rho}_j)\}$ are the programmable phases used for the fiber-array beam focusing (projection) onto the target located at the plane $z=L$, $\{v_j(t)\}$ are the controllable phase shifts used for compensation of the atmospheric-turbulence-induced piston-type phase aberrations $\{\Delta_j^{at}(t)\}$ (target-plane phase locking), and $\{u_j(\boldsymbol{\rho}_j, t)\}$ are the local wavefront phase modulations introduced, e.g., by the x and y fiber-tip actuators incorporated into the fiber collimators.¹² We assume that the piston-type phase components $\{\bar{u}_j(t)\}$ of the phase modulations $\{u_j(\boldsymbol{\rho}_j, t)\}$, defined as the integrals of functions $\{u_j(\boldsymbol{\rho}_j, t)\}$ over the corresponding subaperture areas, equal zero for all indexes j .

2.2 Performance Metrics: Local Wavefront Tilt Measurements

As described in the introduction, the local PIB metrics $\{J_j\}$, $j = 1, \dots, N_{sub}$, are measured by means of the fiber-coupled photodetectors (see Fig. 1). The amount of the received power J_j is inversely proportional to the displacement of the j th fiber-tip center in respect to local displacements x_j^c and y_j^c of a focal-spot centroid from its reference position (the local center coordinates). The displacements x_j^c and y_j^c are directly proportional to local tilts or angular orientation components α_j^x and α_j^y . Assuming $I_j^F(\boldsymbol{\kappa}_j)$ is the input intensity distribution at the plane of the j th fiber tip (focal plane), $\boldsymbol{\kappa}_j = \{\kappa_j^x, \kappa_j^y\} = \mathbf{q} - \mathbf{q}_j$, $\mathbf{q} = \{q_x, q_y\}$ is the spatial-frequency radius vector in the focal plane, and \mathbf{q}_j is the center of the focal plane coinciding with the local center coordinates \mathbf{r}_j , the focal-spot centroid coordinates are given by¹⁷

$$x_j^c \equiv \frac{\int \kappa_j^x I_j^F(\kappa_j^x, \kappa_j^y) d\kappa_j^x d\kappa_j^y}{\int I_j^F(\kappa_j^x, \kappa_j^y) d\kappa_j^x d\kappa_j^y} = F\alpha_j^x, \quad y_j^c \equiv \frac{\int \kappa_j^y I_j^F(\kappa_j^x, \kappa_j^y) d\kappa_j^x d\kappa_j^y}{\int I_j^F(\kappa_j^x, \kappa_j^y) d\kappa_j^x d\kappa_j^y} = F\alpha_j^y, \quad (5)$$

where F is the focal distance of the fiber-collimator lens. For simplicity of notations, we omit the time dependence of the corresponding dynamic variables from the equations. The local tilts in Eq. (5) are defined through the x and y subaperture-averaged local phase gradients (slopes) $s_j^x = k\alpha_j^x$ and $s_j^y = k\alpha_j^y$ given by

$$s_j^x = \frac{1}{S_{sub}} \int_{\Omega_j} \frac{\partial \varphi}{\partial x}(x, y) dx dy, \quad s_j^y = \frac{1}{S_{sub}} \int_{\Omega_j} \frac{\partial \varphi}{\partial y}(x, y) dx dy \quad (j = 1, \dots, N_{sub}), \quad (6)$$

where $S_{sub} = \pi d^2/4$ is the subaperture area, $k = 2\pi/\lambda$ is the optical wavenumber, and λ is the wavelength.

In practice, the focal-spot centroid displacements $\{x_j^c\}$ and $\{y_j^c\}$ are measured through SPGD maximization of the local PIB metrics $\{J_j\}$, which are given as the total projected power of the intensity distributions $\{I_j^F(\boldsymbol{\kappa}_j)\}$ inside the corresponding fiber-core areas. The metric maximization is performed using controllable rapid displacement of the tip of the delivery fiber. The subsequently calculated from Eq. (5) local tilts $\{\alpha_j^x\}$ and $\{\alpha_j^y\}$ or, alternatively, local slopes $\{s_j^x\}$ and $\{s_j^y\}$ are then used to compute the instructions for the following AO control.

2.3 Phase Locking and Higher Order Phase Aberration Compensation

The slopes retrieved do not contain explicit information about the local atmospheric-turbulence-induced pistons. In order to perform the target-plane phase locking of the outgoing array of beamlets, we need to find an algorithm that would permit calculation of local piston-type phase aberrations from the slopes. One of the simplest (though not necessarily optimal) solutions to the problem is the following. First, based on the slope measurements, we perform a reconstruction of the wavefront phase over the entire densely-packed aperture of diameter D , and then from a reconstructed wavefront we calculate the piston-type aberrations; the corresponding procedures are detailed in Sections 3 and 4 and further verified in Section 5.

Higher order local aberrations such as local tilts, defoci, and beyond can, in principle, be computed and mitigated from the reconstructed wavefront as well. To compensate either low-order, or high-order, or both orders of local aberrations, one can use either/both the x - y - z fiber-tip actuators¹² for tilts and defocus or/and the multi-pixel LC phase SLM or AO controllable deformable mirrors for higher order aberration compensations. In the present paper, we limit our analysis to compensation of the local tips and tilts only. These tilts are measured through the local PIB metrics $\{J_j\}$, $j = 1, \dots, N_{sub}$, as described in Section 2.2.

3. MODAL WAVEFRONT RECONSTRUCTION: MATHEMATICAL MODEL

Since the early works,¹⁸⁻²⁰ wavefront reconstruction from its gradients is one of the largely studied tasks in adaptive optics (AO), mostly due to a wide use of the Shack-Hartmann-type sensors.^{8,9} Traditionally, two approaches by which the wavefront may be represented are identified: modal and zonal estimations (see Ref. [21] and references therein). Zonal algorithms build a discrete phase field in the vicinity of the measured points; the phase data in between the

measured points are interpolated. Modal algorithms approximate the wavefront phase by a series of a number of aperture response functions (modes).

In adaptive optics, modal algorithms are prevalent, with different choices of basis response functions and algorithms. One of the most widespread techniques is the least squares estimation algorithm.^{14,22} Although there are further advances in reconstruction procedures that provide more accurate results,^{23–32} in the present work we consider only the least squares estimation because it can be applied to the phase reconstruction without *a priori* knowledge of the phase statistics and also because it has no apparent restriction on the form, geometry, or the number of subapertures.²²

3.1 Least Squares Estimation Algorithm

We use detailed in Ref. [14] modal wavefront reconstruction procedure based on the least squares minimization algorithm. This procedure is described as follows.

At the pupil plane of the sparse aperture of diameter D , defined here by a circle of the smallest diameter that contains all the subapertures within it (the circumscribed circle), the input wavefront $\varphi(\mathbf{r})$ can be decomposed into a set of orthogonal response functions. As basis response functions, different polynomials such as Zernike polynomials^{33,34} and atmospheric Karhunen-Loeve functions are used.^{14,35} In the present work we use the orthonormal annular Zernike polynomials $\{Z_l(\mathbf{r})\}$.^{36,37} The polynomial expansion of the arbitrary function $\varphi(\mathbf{r})$ over a circle of diameter D is therefore given by³⁴

$$\varphi(\mathbf{r}) = \sum_{l=0}^{\infty} a_l Z_l(\mathbf{r}), \quad (7)$$

where the index l orders the polynomials and $\{a_l\}$ are the phase aberration coefficients,

$$a_l = \frac{1}{S_M} \int_{\Omega} \varphi(\mathbf{r}) Z_l(\mathbf{r}) \mathbf{d}\mathbf{r}, \quad (8)$$

$\mathbf{d}\mathbf{r} = r dr d\theta$, Ω is the circular monolithic aperture of diameter D , and $S_M = \pi D^2/4$. Note that for simplicity of notations we write $\{Z_l(\mathbf{r})\}$ instead of $\{Z_l(2\mathbf{r}/D)\}$ defined on the unit circle.

The wavefront is sensed by an array of N_{sub} subapertures through measurements of the subaperture-averaged x and y tilts $\alpha_j^x = s_j^x/k$ and $\alpha_j^y = s_j^y/k$, where s_j^x and s_j^y are the subaperture-averaged wavefront slopes given by Eqs. (6). Substituting Eq. (7) into Eqs. (6), we obtain the following expressions for the slopes:

$$s_j^x = \frac{1}{S_{sub}} \sum_{l=1}^{\infty} a_l \int_{\Omega_j} \frac{\partial Z_l}{\partial x}(x, y) dx dy = \sum_{l=1}^{\infty} a_l G_{j,l}^x, \quad s_j^y = \frac{1}{S_{sub}} \sum_{l=1}^{\infty} a_l \int_{\Omega_j} \frac{\partial Z_l}{\partial y}(x, y) dx dy = \sum_{l=1}^{\infty} a_l G_{j,l}^y, \quad (j = 1, \dots, N_{sub}), \quad (9)$$

where $G_{j,l}^x \equiv S_{sub}^{-1} \int_{\Omega_j} [\partial Z_l(x, y)/\partial x] dx dy$ and $G_{j,l}^y \equiv S_{sub}^{-1} \int_{\Omega_j} [\partial Z_l(x, y)/\partial y] dx dy$. Here we took into account that the derivatives of the zero mode Z_0 , piston, equal zero. In the matrix form, Eqs. (9) can be rewritten as

$$\mathbf{s} = \mathbf{G}\mathbf{a}, \quad (10)$$

where $\mathbf{s} = \{s_1^x, s_1^y, \dots, s_j^x, s_j^y, \dots, s_{N_{sub}}^x, s_{N_{sub}}^y\}$ is the slope column vector, $\mathbf{a} = \{a_1, \dots, a_l, \dots\}$ is an infinite column vector of exact aberration coefficients, and \mathbf{G} is a $2N_{sub}$ -by-infinity matrix containing the subaperture-averaged gradients of Zernike functions,

$$\mathbf{G} = \begin{pmatrix} G_{1,1}^x & \cdots & G_{1,l}^x & \cdots \\ G_{1,1}^y & \cdots & G_{1,l}^y & \cdots \\ \vdots & \ddots & \vdots & \ddots \\ G_{j,1}^x & \cdots & G_{j,l}^x & \cdots \\ G_{j,1}^y & \cdots & G_{j,l}^y & \cdots \\ \vdots & \ddots & \vdots & \ddots \\ G_{N_{sub},1}^x & \cdots & G_{N_{sub},l}^x & \cdots \\ G_{N_{sub},1}^y & \cdots & G_{N_{sub},l}^y & \cdots \end{pmatrix}. \quad (11)$$

Assuming that we know the slope vector \mathbf{s} from the measurements of the subaperture-averaged x and y coordinates of focal spots (see Section 2.2) and the subaperture-averaged response function derivatives $\{G_{j,l}^x\}$ and $\{G_{j,l}^y\}$, calculated either analytically or numerically, we would like now to estimate the aberration coefficients \mathbf{a} .

Equations (10) cannot be solved with an infinite number of modes since it is an underdetermined system for $N > 2N_{sub}$; instead, one should replace infinity with $N \leq 2N_{sub}$ and seek to obtain the first N coefficients of the aberration coefficient column vector \mathbf{a} . However, due to the fact that the measured values of local slopes contain gradient components from the remaining ($> N$) high-order response functions (not taking into account other noise sources), those coefficients cannot be found exactly (see Section 3.2). Instead, one should seek for approximated solutions. In this case, the wavefront phase in search is approximated as

$$\phi(\mathbf{r}) = \sum_{l=1}^N b_l Z_l(\mathbf{r}), \quad (12)$$

where $\{b_l\}$ are the estimated phase aberration coefficients. Repeating the procedure, one obtain

$$\mathbf{s} = \tilde{\mathbf{G}}\mathbf{b}, \quad (13)$$

where $\mathbf{b} = \{b_1, \dots, b_l, \dots, b_N\}$ and $\tilde{\mathbf{G}}$ is a $2N_{sub}$ -by- N matrix coinciding with the first N columns of the matrix \mathbf{G} .

Let us suppose $N = 2N_{sub}$, that is, we have N -by- N matrix equation (13) which can be solved by taking the matrix inverse to obtain

$$\mathbf{b} = \tilde{\mathbf{G}}^{-1}\mathbf{s}, \quad (14)$$

where $\tilde{\mathbf{G}}^{-1}$ is the inverse of the N -by- N square matrix $\tilde{\mathbf{G}}$. Note that solution (14) exists only if matrix $\tilde{\mathbf{G}}$ is invertible, that is, the columns of $\tilde{\mathbf{G}}$ are linearly independent (non-singular or non-degenerate matrix).

Suppose now we have $N < 2N_{sub}$, that is, the system is overdetermined. In this case the system of linear equations (13) lacks a unique solution. Let $\tilde{\mathbf{G}}\mathbf{b} - \mathbf{s} = \mathbf{res}$, where \mathbf{res} is a residual column vector, and use calculus to minimize the length of \mathbf{res} , $\|\tilde{\mathbf{G}}\mathbf{b} - \mathbf{s}\|$. The standard least squares solution of Eq. (13) is³⁸

$$\mathbf{b} = \tilde{\mathbf{G}}^+\mathbf{s}, \quad (15)$$

where $\tilde{\mathbf{G}}^+ = (\tilde{\mathbf{G}}^T\tilde{\mathbf{G}})^{-1}\tilde{\mathbf{G}}^T$ is the pseudoinverse or the generalized inverse of the matrix $\tilde{\mathbf{G}}$, $\tilde{\mathbf{G}}^T$ is the transpose of matrix $\tilde{\mathbf{G}}$ and $(\tilde{\mathbf{G}}^T\tilde{\mathbf{G}})^{-1}$ is the inverse of the N -by- N matrix $\tilde{\mathbf{G}}^T\tilde{\mathbf{G}}$. We note that if both columns and rows of the matrix $\tilde{\mathbf{G}}$ are linearly independent (that is, for square regular matrices), the pseudoinverse $\tilde{\mathbf{G}}^+$ is just the inverse $\tilde{\mathbf{G}}^{-1}$, and the solutions (14) and (15) coincide. This means that solution (15) is applicable to the case $N = 2N_{sub}$ as well.

3.2 Cross Coupling and Aliasing of Wavefront Estimation

As explicitly shown in Ref. [14], the lower-order ($< N$) estimated coefficients $\{b_l\}$ are influenced by the higher order ($> N$) coefficients $\{a_l\}$. This is the so-called problem of cross coupling of aberrations (lack of orthogonality of its column vectors) and aliasing of aberrations (lack of linear independence of its column vectors).^{39,40} The linear correlation (aliasing) between the columns in the gradient matrix originates from the symmetry of subaperture configurations.⁴⁰ Note that the use of asymmetrical or randomized subaperture geometries can reduce the effect.⁴¹ The cross coupling, in its turn, is attributable to the nonorthogonality of the derivatives of the basis response functions. In order to avoid this problem, one can in principle choose a set of polynomials whose derivatives are orthogonal over the locations of the measurements (subapertures).³⁹ When using Zernike polynomials as basis response functions, the mode cross coupling already occurs when one tries to estimate modes higher than astigmatism, and in order to maintain the quality of the low-order mode estimates it is desirable to minimize the number of estimated (reconstructed) modes.³⁹ Regardless, a complete elimination of the remaining error does not seem feasible.

3.3 Modal Wavefront Reconstruction Error

Knowing estimated phase aberration coefficients $\{b_l\}$, one can reconstruct the phase $\phi(\mathbf{r})$ using Eq. (12). As a modal wavefront reconstruction efficiency characteristic, let us define the ensemble- or atmospheric-averaged mean square error,

$$\langle \sigma_{\text{WR}}^2 \rangle = \frac{1}{S_M} \left\langle \int_{\Omega} [\varphi(\mathbf{r}) - \phi(\mathbf{r})]^2 d\mathbf{r} \right\rangle. \quad (16)$$

Here we assume that the sparse-aperture-averaged values of both original and reconstructed wavefronts equal zero, i.e., $\int_{\Omega} \varphi(\mathbf{r}) d\mathbf{r} = 0$ and $\int_{\Omega} \phi(\mathbf{r}) d\mathbf{r} = 0$.

4. PISTON AND TILT ABERRATION COMPENSATION

4.1 Piston Phase Retrieval and Compensation

Consider decomposition of phase aberrations $\{\varphi_j(\boldsymbol{\rho}_j)\}$ inside each subaperture using the set of Zernike response functions $\{Z_l(\boldsymbol{\rho}_j)\}$ defined on the subaperture areas $\{\Omega_j\}$, $j = 1, \dots, N_{\text{sub}}$, that is,

$$\varphi(\mathbf{r}) = \sum_{j=1}^{N_{\text{sub}}} \varphi_j(\boldsymbol{\rho}_j) = \sum_{j=1}^{N_{\text{sub}}} \left[M(\boldsymbol{\rho}_j) \Delta_j^{\text{at}} + \sum_{l=1}^{\infty} a_{j,l} Z_l(\boldsymbol{\rho}_j) \right], \quad (17)$$

where $\{\Delta_j^{\text{at}}\}$ are the piston-type phase aberration components inside the system subapertures and $\{a_{j,l}\}$ are the phase aberration coefficients corresponding to the spatially-varying phase aberration components $\{\varphi_j^{\text{at}}(\boldsymbol{\rho}_j)\}$.² From the original wavefront $\varphi(\mathbf{r})$, the local piston-type aberrations are defined as

$$\Delta_j^{\text{at}} = \frac{1}{S_{\text{sub}}} \int_{\Omega_j} \varphi(\mathbf{r}) d\mathbf{r} \quad (j = 1, \dots, N_{\text{sub}}). \quad (18)$$

Note that since calculation of pistons $\{\Delta_j^{\text{at}}\}$ require *a priori* knowledge of $\varphi(\mathbf{r})$, they can be referred to as “true” pistons, and compensation of the atmospheric turbulence-induced piston-type phase aberrations $\{\Delta_j^{\text{at}}\}$ is correspondingly referred to as “true” piston compensation.

The estimated piston-type aberrations that can be retrieved from the reconstructed phase $\phi(\mathbf{r})$ are in the same way defined as

$$\Delta_j^{\text{est}} = \frac{1}{S_{\text{sub}}} \int_{\Omega_j} \phi(\mathbf{r}) d\mathbf{r} \quad (j = 1, \dots, N_{\text{sub}}). \quad (19)$$

Compensation of estimated phase shifts $\{\Delta_j^{\text{est}}\}$ by means of the controllable phase shifts $\{v_j(t)\}$ is referred to here as the piston aberration component compensation based on the measured subaperture-averaged wavefront slopes, or the partial piston compensation, to be short.

4.2 Residual Piston Phase Errors

After true piston compensation, the residual (uncompensated) phase defined on the subaperture areas is therefore written as

$$\delta_{\text{true}}(\mathbf{r}) = \sum_{j=1}^{N_{\text{sub}}} [\varphi_j(\boldsymbol{\rho}_j) - M(\boldsymbol{\rho}_j) \Delta_j^{\text{at}}] = \sum_{j=1}^{N_{\text{sub}}} \delta_j^{\text{true}}(\boldsymbol{\rho}_j) = \sum_{j=1}^{N_{\text{sub}}} \varphi_j^{\text{at}}(\boldsymbol{\rho}_j), \quad (20a)$$

and for the partial piston compensation it is correspondingly given by

$$\delta_{\text{est}}(\mathbf{r}) = \sum_{j=1}^{N_{\text{sub}}} [\varphi_j(\boldsymbol{\rho}_j) - M(\boldsymbol{\rho}_j) \Delta_j^{\text{est}}] = \sum_{j=1}^{N_{\text{sub}}} \delta_j^{\text{est}}(\boldsymbol{\rho}_j), \quad (20b)$$

where $\delta_j^{\text{true}}(\boldsymbol{\rho}_j)$ and $\delta_j^{\text{est}}(\boldsymbol{\rho}_j)$ are the corresponding residual phase aberrations at the j th subaperture.

One way to characterize the efficiency of the wavefront reconstruction technique with subsequent pistons' retrieval is to calculate the atmospheric-averaged values of the mean square residual phase errors, which are respectively defined as²

$$\langle \sigma_{\text{PL}}^2 \rangle_{\text{true}} = \frac{1}{S_C} \left\langle \sum_{j=1}^{N_{\text{sub}}} \int_{\Omega_j} [\varphi_j(\boldsymbol{\rho}_j) - M(\boldsymbol{\rho}_j) \Delta_j^{\text{at}}]^2 d\boldsymbol{\rho}_j \right\rangle = \frac{1}{S_C} \sum_{j=1}^{N_{\text{sub}}} \int_{\Omega_j} \langle [\delta_j^{\text{true}}(\boldsymbol{\rho}_j)]^2 \rangle d\boldsymbol{\rho}_j, \quad (21a)$$

$$\langle \sigma_{\text{PL}}^2 \rangle_{\text{est}} = \frac{1}{S_C} \left\langle \sum_{j=1}^{N_{\text{sub}}} \int_{\Omega_j} [\varphi_j(\mathbf{p}_j) - M(\mathbf{p}_j) \Delta_j^{\text{est}}]^2 d\mathbf{p}_j \right\rangle = \frac{1}{S_C} \sum_{j=1}^{N_{\text{sub}}} \int_{\Omega_j} \langle [\delta_j^{\text{est}}(\mathbf{p}_j)]^2 \rangle d\mathbf{p}_j. \quad (21b)$$

Note that the introduced errors [Eqs. (16) and (21)] are quantifiable only if we know the original wavefront explicitly. If $\varphi(\mathbf{r})$ is unknown, other criteria should be used to estimate the piston retrieval and compensation (phase locking) efficiency, such as, for example, the Strehl ratios $St = I_F(0) / I_F^{\text{dif}}(0)$ (normalized on-axis intensity in the Fourier plane) and $St_{\text{max}} = \max I_F / I_F^{\text{dif}}(0)$ (normalized maximum value of intensity in the Fourier plane).

4.3 Local Tilt Compensation

Suppose AO control at each circular subaperture of diameter d additionally includes compensation of local tilts, which are defined through the first and second Zernike polynomials $Z_1(\mathbf{p}_j) = (4/d)(x - x_j)$ and $Z_2(\mathbf{p}_j) = (4/d)(y - y_j)$. Assuming phase (17) consists of first or second Zernike polynomials only, from the tilt definitions and Eqs. (6) we obtain the following relationships for the “true” tilts: $\alpha_j^{x, \text{true}} = (4/d)a_{j,1}/k$ and $\alpha_j^{y, \text{true}} = (4/d)a_{j,2}/k$, where $a_{j,1}$ and $a_{j,2}$ are the phase aberration coefficients. Therefore, true phase aberrations $\{\varphi_j(\mathbf{p}_j)\}$ defined on the subaperture areas $\{\Omega_j\}$ are given by

$$\varphi_j(x - x_j, y - y_j) = \Delta_j^{\text{at}} + k[\alpha_j^{x, \text{true}}(x - x_j) + \alpha_j^{y, \text{true}}(y - y_j)] + \delta_j^{\text{nl, true}}(x - x_j, y - y_j), \quad (22a)$$

where $\delta_j^{\text{nl, true}}(x - x_j, y - y_j) = \delta_j^{\text{nl, true}}(\mathbf{p}_j)$ is the true nonlinear residual phase aberration at the j th subaperture. Analogously, for the estimated phase aberrations we write

$$\phi_j(x - x_j, y - y_j) = \Delta_j^{\text{est}} + k[\alpha_j^{x, \text{est}}(x - x_j) + \alpha_j^{y, \text{est}}(y - y_j)] + \delta_j^{\text{nl, est}}(x - x_j, y - y_j), \quad (22b)$$

where $\alpha_j^{x, \text{est}} = x_j^c/F$ and $\alpha_j^{y, \text{est}} = y_j^c/F$ are the estimated wavefront phase tilts calculated from the beamlets’ centroid measurements (5) through the local PIB metric optimization and $\delta_j^{\text{nl, est}}(\mathbf{p}_j)$ is the estimated residual phase aberration at the j th subaperture. Note that the estimated wavefront tilts are measured with contributions from high-order Zernike modes,⁴² so they differ from the true tilts. In both cases, the atmospheric-averaged values of the mean square nonlinear residual phase errors $\langle \sigma_{\text{PL+TT}}^2 \rangle_{\text{true}}$ and $\langle \sigma_{\text{PL+TT}}^2 \rangle_{\text{est}}$ are defined analogously as in Eqs. (21).

5. NUMERICAL RESULTS

In the first part of our numerical simulations presented in Sections 5.1 and 5.2, the atmospheric turbulence was accounted for by using a single phase screen $\varphi(\mathbf{r})$ of Kolmogorov statistics located at the fiber-array pupil plane (pupil-plane phase screen). In Section 5.3, in order to model the spatially distributed turbulence, we used 20 phase screens equidistantly distributed along the laser beam propagation path. Atmospheric turbulence strength was accounted for by varying the Fried parameter r_0 .⁴³ Generation of phase screens was performed on a numerical grid with $N \times N$ points ($N = 1024$) using spectral approach.^{44–47} The densely-packed aperture of diameter D was located in the grid central area of diameter $(6/8)N$ pixels. To obtain statistically averaged values of the examined metrics (e.g., mean square phase errors), the computations were repeated with a set of 100 independent phase screen realizations, and the obtained metric values were averaged.

5.1 Modal Wavefront Reconstruction

For the pupil-plane phase screen model, we know $\varphi(\mathbf{r})$ explicitly, so the analysis is straightforward. To measure $2N_{\text{sub}}$ subaperture-averaged phase gradients $\{s_j^x\}$ and $\{s_j^y\}$ inside each subaperture, we take derivatives to x and y on $\varphi(\mathbf{r})$ and spatially average them within each subaperture. The subaperture-averaged gradients of Zernike response functions $\{G_{j,l}^x\}$ and $\{G_{j,l}^y\}$ are calculated accordingly. Numerically, least squares solution of Eq. (13) for $N \leq 2N_{\text{sub}}$ is found by performing the singular-value decomposition of the matrix $\tilde{\mathbf{G}}$ and then applying the singular value backsubstitution procedure in order to find \mathbf{b} ; both routines, named `svdcmp` and `svbksb`, are given in Ref. [48]. After computing estimated phase aberration coefficients $\{b_l\}$, the estimated phase $\phi(\mathbf{r})$ was reconstructed using Eq. (12).

The atmospheric-averaged mean square wavefront reconstruction (WR) error (16) was calculated for different system architectures and parameters; dependences of the normalized errors $\langle \hat{\sigma}_{\text{WR}}^2(N) \rangle = \langle \sigma_{\text{WR}}^2(N) \rangle / \langle \sigma_{\text{WR}}^2(N=0) \rangle$, where $\langle \sigma_{\text{WR}}^2(N=0) \rangle = (1/S_M) \langle \int_{\Omega} \varphi^2(\mathbf{r}) d\mathbf{r} \rangle$, on a number of reconstructed modes N are shown by solid lines in Fig. 2(a). For the sake of comparativeness, the same error was calculated with $\varphi_N(\mathbf{r}) = \sum_{l=0}^N a_l Z_l(\mathbf{r})$ instead of $\phi(\mathbf{r}) = \sum_{l=0}^N b_l Z_l(\mathbf{r})$ [see Eq. (12)], where the phase aberration coefficients $\{a_l\}$ were calculated directly from the original wavefront $\phi(\mathbf{r})$ [see Eq. (8)]; the corresponding dependence of this error, referred to as the true wavefront reconstruction error $\langle \hat{\sigma}_{\text{WR}}^2 \rangle_{\text{true}}$, is shown in Fig. 2(a) by the dashed line.

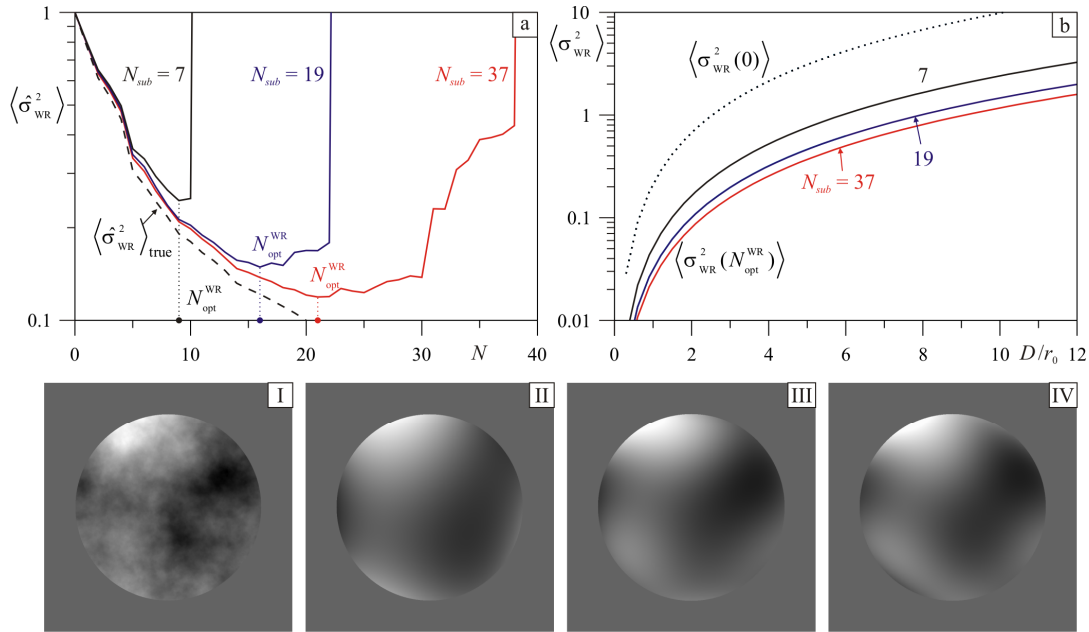


Figure 2. (a) Dependences of the normalized ensemble-averaged mean square wavefront reconstruction error $\langle \hat{\sigma}_{\text{WR}}^2 \rangle$ on the number of reconstructed Zernike modes N for a different number of subapertures N_{sub} with fixed fiber-array aperture diameter D and $D/r_0 = 3$. (b) Dependences of the mean square error $\langle \sigma_{\text{WR}}^2 \rangle$ [rad²] on D/r_0 for a different number of subapertures N_{sub} . In (b), dotted lines are for $N = 0$ (no compensation) and solid lines are for $N = N_{\text{opt}}^{\text{WR}}(N_{\text{sub}})$. Inserts at the bottom marked by (I)–(IV) represent phase distributions: (I) is the original phase; (II)–(IV) are the reconstructed wavefronts for $N_{\text{sub}} = 7$ and $N = 9$ (II), $N_{\text{sub}} = 19$ and $N = 16$ (III), and $N_{\text{sub}} = 37$ and $N = 21$ (IV).

As can be seen from the figure, an increase of the subaperture number (that is, the number of measured phase gradients over the same area) leads to a possibility to recover a larger number of Zernike polynomials with the smaller WR error. On the other hand, due to the contribution of aliasing and cross coupling aberration terms, for sufficiently large N the error increases abruptly, and the reconstruction technique fails. For a specific system architecture configuration, the optimal wavefront reconstruction is said to be achieved for an optimal $N = N_{\text{opt}}^{\text{WR}}$ that results in the smallest WR error.¹⁴

From Fig. 2(a), $N_{\text{opt}}^{\text{WR}}$ is calculated for each configuration; the results are shown in Table 1.

Dependences of $\langle \hat{\sigma}_{\text{WR}}^2 \rangle$ on D/r_0 for a different number of subapertures N_{sub} are shown in Fig. 2(b). Interestingly, for the fixed N_{sub} , the “efficiency” ratio $\langle \hat{\sigma}_{\text{WR}}^2 \rangle = \langle \sigma_{\text{WR}}^2(N = N_{\text{opt}}^{\text{WR}}) \rangle / \langle \sigma_{\text{WR}}^2(N = 0) \rangle$ is proven to be constant over the whole

tested interval of D/r_0 ; this ratio is calculated in Table 2 for a set of N_{sub} considered. Moreover, the dependence $\langle \hat{\sigma}_{WR}^2(N) \rangle$ in Fig. 2(a) appears to be identical for all tested D/r_0 range. This is quite understandable since (at least for a pupil-plane phase-screen model) the change in D/r_0 results in the linearly proportional change of the measured slopes, and correspondingly in the linearly proportional change of the reconstructed Zernike coefficients.

Table 1. Optimal number of reconstruction modes for adaptive array of fiber collimators with a different number of subapertures N_{sub} .

N_{sub}	N_{opt}^{WR}	N_{opt}^{PL}
7	9	8
19	16	16
37	21	30

5.2 Phase Locking and Tilt Compensation

Efficiency of the wavefront reconstruction technique with subsequent pistons' retrieval in fiber-array beam director systems is evaluated through the mean square residual phase errors $\langle \sigma_{PL}^2 \rangle_{true}$ and $\langle \sigma_{PL}^2 \rangle_{est}$ [see Eqs. (21a) and (21b), where the estimated piston-type aberrations are given by Eq. (19)]. In Fig. 3(a), solid lines represent $\langle \hat{\sigma}_{PL}^2 \rangle_{est} = \langle \sigma_{PL}^2(N) \rangle_{est} / \langle \hat{\sigma}_{PL}^2(N=0) \rangle_{est}$ for phase locking through the least squares minimization, and dashed lines

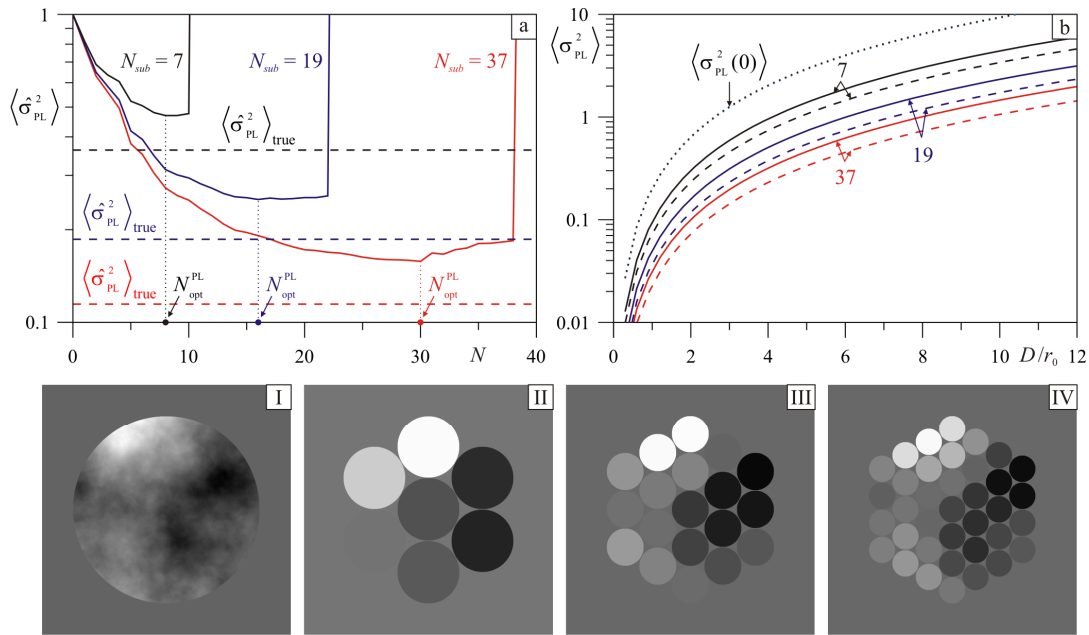


Figure 3. (a) Dependences of the normalized ensemble-averaged mean square residual error $\langle \hat{\sigma}_{PL}^2 \rangle_{est}$ (solid lines) on the number of reconstructed Zernike modes N for a different number of subapertures N_{sub} with fixed fiber-array aperture diameter D and $D/r_0 = 3$. Horizontal dashed lines indicate $\langle \hat{\sigma}_{PL}^2 \rangle_{true}$ for a different number of subapertures (from top to bottom): $N_{sub} = 7, 19$, and 37 . (b) Dependences of the mean square errors $\langle \hat{\sigma}_{PL}^2(N=0) \rangle_{est} = \langle \sigma_{PL}^2(N=0) \rangle_{true}$ (dotted lines), $\langle \hat{\sigma}_{PL}^2(N=N_{opt}^{PL}) \rangle_{est}$ (solid lines), and $\langle \hat{\sigma}_{PL}^2 \rangle_{true}$ (dashed lines) on D/r_0 for a different number of subapertures N_{sub} . Inserts at the bottom marked by (I)–(IV) represent phase distributions: (I) is the original phase and (II)–(IV) are the retrieved pistons for $N_{sub} = 7$ and $N = 8$ (II), $N_{sub} = 19$ and $N = 16$ (III), and $N_{sub} = 37$ and $N = 30$ (IV).

show $\langle \hat{\sigma}_{\text{PL}}^2 \rangle_{\text{true}}$, which are not dependent on the number of the reconstructed modes N but are different for a different number of fiber collimators N_{sub} [see Eq. (21a)]. Again, for sufficiently large N , the error $\langle \hat{\sigma}_{\text{PL}}^2 \rangle_{\text{est}}$ sharply increases and the reconstruction technique fails. Note that the optimal number of the reconstructed modes $N_{\text{opt}}^{\text{PL}}$ that results in the smallest phase-locking (PL) error do not coincide with $N_{\text{opt}}^{\text{WR}}$ (see Table 1).

Dependences of $\langle \sigma_{\text{PL}}^2 \rangle_{\text{true}}$ and $\langle \sigma_{\text{PL}}^2 \rangle_{\text{est}}$ on D/r_0 are shown in Fig. 3(b) by dashed and solid lines, respectively. Analogously to $\langle \hat{\sigma}_{\text{WR}}^2(N) \rangle$, the efficiency ratios $\langle \hat{\sigma}_{\text{PL}}^2 \rangle_{\text{true}}$ and $\langle \hat{\sigma}_{\text{PL}}^2 \rangle_{\text{est}}$ are constant in the examined range of D/r_0 (see Table 2). The results presented indicate a significant PL error reduction and the corresponding gain in the laser beam power projection with the increase of a number of the phase-locked subapertures N_{sub} in the coherent fiber-array-based systems.

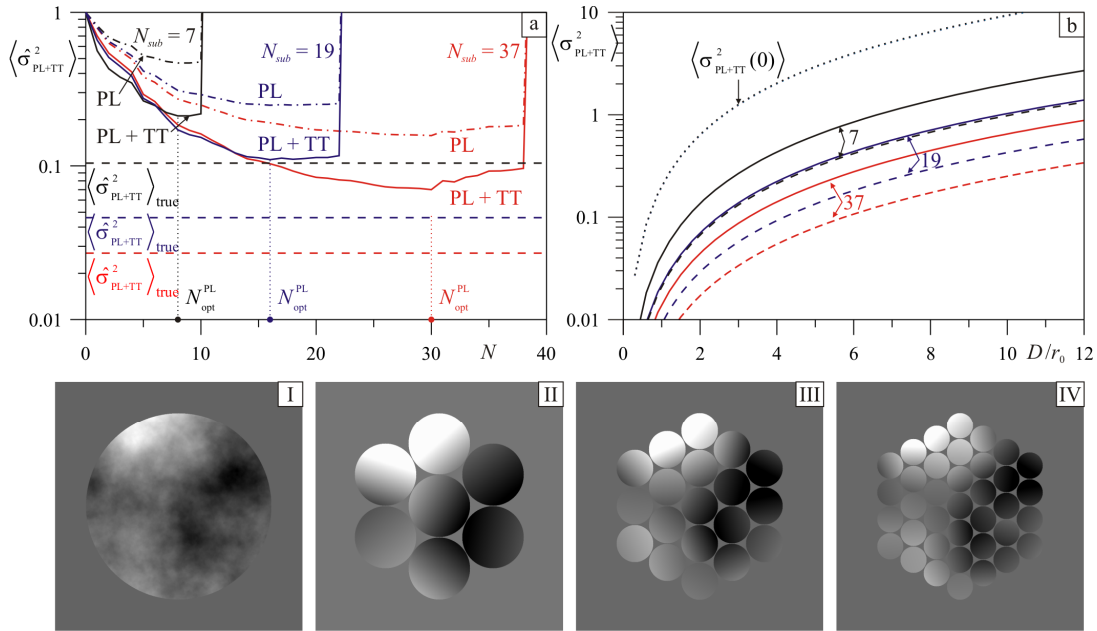


Figure 4. (a) Dependences of the normalized ensemble-averaged mean square residual error $\langle \hat{\sigma}_{\text{PL+TT}}^2 \rangle_{\text{est}}$ for phase locking plus local tip and tilt compensation (“PL + TT”, solid lines) on the number of reconstructed Zernike modes N for a different number of subapertures N_{sub} with fixed fiber-array aperture diameter D and $D/r_0 = 3$. Horizontal dashed lines indicate $\langle \hat{\sigma}_{\text{PL+TT}}^2 \rangle_{\text{true}}$ for phase locking plus local tip and tilt compensation and for a different number of subapertures (from top to bottom): $N_{\text{sub}} = 7, 19$, and 37 . For comparison, curves $\langle \hat{\sigma}_{\text{PL}}^2 \rangle_{\text{est}}$ from Fig. 3(a) are shown in (a) as well (“PL”, dot-dashed lines). (b) Corresponding dependences of the mean square errors $\langle \sigma_{\text{PL+TT}}^2(N=0) \rangle_{\text{true/est}} = \langle \sigma_{\text{PL}}^2(N=0) \rangle_{\text{true/est}}$ (dotted lines), $\langle \sigma_{\text{PL+TT}}^2(N=N_{\text{opt}}^{\text{PL}}) \rangle_{\text{est}}$ (solid lines), and $\langle \sigma_{\text{PL+TT}}^2 \rangle_{\text{true}}$ (dashed lines) on D/r_0 for a different number of subapertures N_{sub} . Inserts marked by (I)–(IV) represent phase distributions: (I) is the original phase and (II)–(IV) are the reconstructed pistons plus local tilts for $N_{\text{sub}} = 7$ and $N = 8$ (II), $N_{\text{sub}} = 19$ and $N = 16$ (III), and $N_{\text{sub}} = 37$ and $N = 30$ (IV).

Consider now a fiber-array beam director with precompensation of tip and tilt components of phase distortion at each subaperture. The atmospheric-averaged dependences of the mean square nonlinear residual phase errors $\langle \hat{\sigma}_{\text{PL+TT}}^2 \rangle_{\text{true}}$

and $\langle \sigma_{\text{PL+TT}}^2 \rangle_{\text{est}}$ on the number of reconstructed Zernike modes N and on D/r_0 ratio for a different number of subapertures N_{sub} are shown in Figs. 4(a) and 4(b), respectively; the corresponding efficiency ratios are given in Table 2. As seen from comparison of Figs. 3 and 4, incorporation of tip and tilt aberration compensation results in a substantial decrease of the residual phase metrics (the system efficiency increase) for all the system configurations considered.

Table 2. Normalized residual phase errors for adaptive control in phased array of fiber collimators.

N_{sub}	Wavefront reconstruction, $\langle \hat{\sigma}_{\text{WR}}^2 \rangle$	Phase locking only		Phase locking plus tilts	
		Reconstructed, $\langle \hat{\sigma}_{\text{PL}}^2 \rangle_{\text{est}}$	True, $\langle \hat{\sigma}_{\text{PL}}^2 \rangle_{\text{true}}$	Reconstructed, $\langle \hat{\sigma}_{\text{PL+TT}}^2 \rangle_{\text{est}}$	True, $\langle \hat{\sigma}_{\text{PL+TT}}^2 \rangle_{\text{true}}$
7	0.26±0.06	0.5±0.1	0.4±0.1	0.21±0.06	0.11±0.02
19	0.15±0.03	0.25±0.05	0.19±0.04	0.11±0.02	0.046±0.005
37	0.12±0.02	0.16±0.02	0.11±0.02	0.07±0.01	0.027±0.002

The impact of the target-plane phase locking as well as local tip/tilt phase aberration compensation on the overall laser beam power delivered onto the target is further illustrated in Fig. 5 representing both the on-axis $St = I_F(0) / I_F^{\text{dif}}(0)$ and $St_{\text{max}} = \max I_F / I_F^{\text{dif}}(0)$ vs. the turbulence strength parameter D/r_0 . These dependences can be used for comparative analysis of various adaptive system configurations characterized by a different number of fiber collimators, the adaptive compensation resolution, and atmospheric turbulence conditions. The advantage of the incorporation of the local tip and tilt compensation capabilities into the coherent fiber-array-based systems considered is quite apparent, which confirms the conclusion derived in Ref. [2]. At the same time, our analysis demonstrate noticeable efficiency reduction of the fiber-array system using the practical phase aberration precompensation technique considered, compared to ideal systems with true aberration compensation.

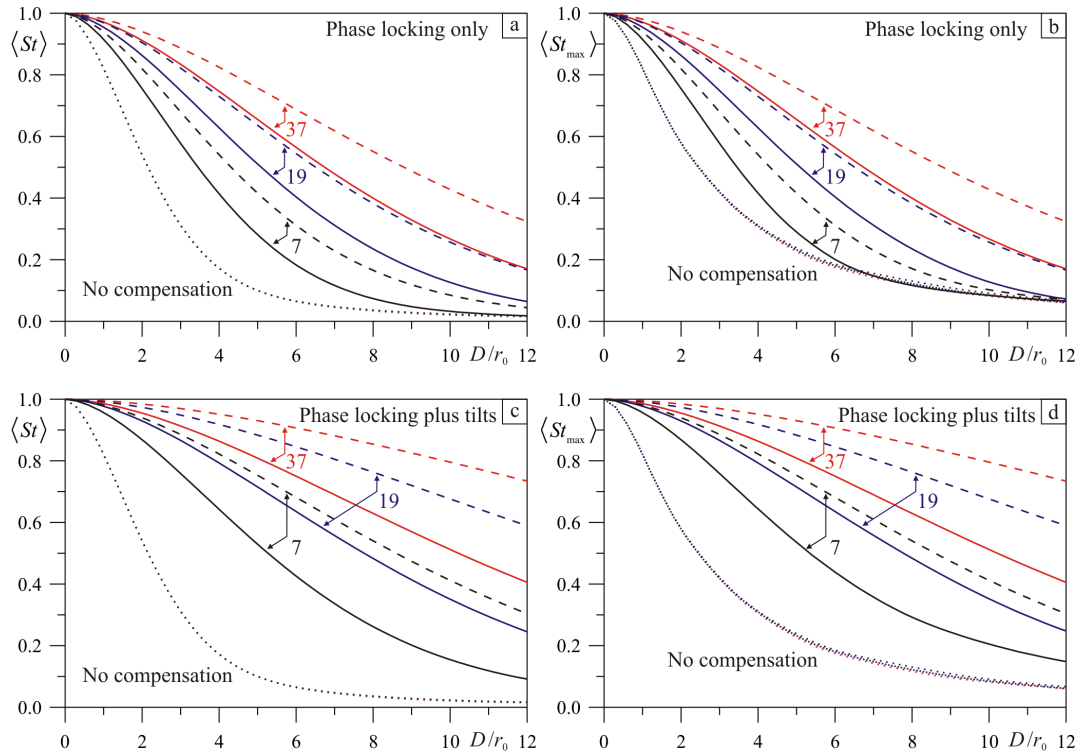


Figure 5. Atmospheric-averaged Strehl metrics $\langle St \rangle$ [(a) and (c)] and $\langle St_{\text{max}} \rangle$ [(b) and (d)] vs. D/r_0 ratio for no compensation [(a)–(d), dotted lines], phase locking only [(a) and (b), solid lines] and phase locking plus local tip and tilt compensation [(c) and (d), solid lines] and a different number of subapertures N_{sub} . Dashed lines represent the corresponding to $\langle St \rangle$ and $\langle St_{\text{max}} \rangle$ “true” Strehl ratios $\langle St \rangle_{\text{true}}$ and $\langle St_{\text{max}} \rangle_{\text{true}}$.

5.3 Wavefront Sensing and Adaptive Control in Spatially Distributed Turbulence

In the second part of our numerical analysis we simulated, to a certain extent, laser beam projection over a long (149 km) near-horizontal propagation path between Mauna Loa (Hawaii Island) and Haleakala (Island of Maui) mountains, as in the Coherent Multi-Beam Atmospheric Transceiver (COMBAT) experiments conducted in February 2010.⁴⁹ As a point-source target, we modeled the laser beacon used in these experiments at the Mauna Loa Observatory, which comprised a single-mode fiber collimator with a clear aperture of 26 mm and the wavelength $\lambda = 1.55 \mu\text{m}$. The sparse-aperture diameter of the receiver telescope D was fixed at 3.67 m, as for the Air Force Advanced Electro-Optical System (AEOS telescope). Since the propagation path simulated is nearly horizontal, the homogeneous turbulence model was used; the turbulence strength was adjusted so that $D/r_0 = 6$. To estimate the efficiency of the adaptive control in phased array of fiber collimators, Strehl ratios $\langle St \rangle$ were calculated; the results are presented in the form of a bar diagram in Fig. 6. These results prove that the wavefront sensing and adaptive control concept presented can be effectively applied for the long-range laser beam projection scenarios characterized by the presence of intensity scintillations of the received wave.

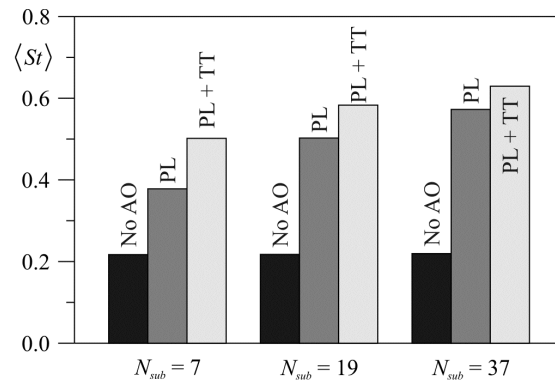


Figure 6. Atmospheric-averaged Strehl metric values $\langle St \rangle$ for adaptive array of fiber collimators operating in distributed turbulence with $D/r_0 = 6$. In this bar diagram, each set of three bars corresponds to a different number of subapertures N_{sub} indicated at the bottom of the bar sets. “No AO” (dark-gray bars) denotes no compensation, “PL” (medium-gray bars) – phase locking only, and “PL + TT” (light-gray bars) – phase locking plus local tip and tilt compensation.

ACKNOWLEDGMENTS

This work was supported by Cooperative Agreement W911NF-06-2-0009 between the U.S. Army Research Laboratory and the University of Maryland, College Park.

REFERENCES

- [1] Vorontsov, M. A. and Lachinova S. L., “Laser beam projection with adaptive array of fiber collimators. I. Basic considerations for analysis,” *J. Opt. Soc. Am. A* 25(8), 1949–1959 (2008).
- [2] Lachinova, S. L. and Vorontsov M. A., “Laser beam projection with adaptive array of fiber collimators. II. Analysis of atmospheric compensation efficiency,” *J. Opt. Soc. Am. A* 25(8), 1960–1973 (2008).
- [3] Vorontsov, M. A., Lachinova, S. L., Beresnev, L. A., and Weyrauch, T., “Obscuration-free pupil-plane phase locking of a coherent array of fiber collimators,” *J. Opt. Soc. Am. A* 27(11), A106–A121 (2010).
- [4] Vorontsov, M. A., Kolosov, V. V., and Kohnle, A., “Adaptive laser beam projection on an extended target: phase- and field-conjugate precompensation,” *J. Opt. Soc. Am. A* 24(7), 1975–1993 (2007).
- [5] Hartmann, J., “Bemerkungen über den Bau und die Justirung von Spektrographen,” *Zt. Instrumentenk.* 20, 47 (1900).
- [6] Hartmann, J., “Objektuntersuchungen,” *Zt. Instrumentenk.* 24, 1 (1904).
- [7] Shack, R. V., and Platt, B. C., “Production and use of a lenticular Hartmann screen,” *J. Opt. Soc. Am.* 61(5), 656 (1971).
- [8] Rousset, G., [Adaptive Optics in Astronomy], F. Roddier, ed., Cambridge University Press, New York, 91–130 (1999).
- [9] Malacara, D., ed., [Optical Shop Testing], 3rd ed., Wiley-Interscience, New York (2007).
- [10] Vorontsov, M. A., Carhart, G. W., and Ricklin, J. C., “Adaptive phase-distortion correction based on parallel gradient-descent optimization,” *Opt. Lett.* 22(12), 907–909 (1997).

- [11] Vorontsov, M. A., Carhart, G. W., Cohen, M., and Cauwenberghs, G., "Adaptive optics based on analog parallel stochastic optimization: analysis and experimental demonstration," *J. Opt. Soc. Am. A* 17(8), 1440–1453 (2000).
- [12] Vorontsov, M. A., Weyrauch, T., Beresnev, L. A., Carhart, G. W., Liu, L., and Aschenbach, K., "Adaptive array of phase-locked fiber collimators: Analysis and experimental demonstration," *IEEE J. Sel. Top. Quantum Electron.* 15(2), 269–280 (2009).
- [13] O'Meara, T. R., "The multidither principle in adaptive optics," *J. Opt. Soc. Am.* 67(3), 306–315 (1977).
- [14] Dai, G.-M., "Modal wave-front reconstruction with Zernike polynomials and Karhunen-Loeve functions," *J. Opt. Soc. Am. A* 13(6), 1218–1225 (1996).
- [15] Vorontsov, M. A., and Kolosov, V. V., "Target-in-the-loop beam control: basic considerations for analysis and wave-front sensing," *J. Opt. Soc. Am. A* 22(1), 126–141 (2005).
- [16] Lachinova, S. L. and Vorontsov, M. A., "Performance analysis of an adaptive phase-locked tiled fiber array in atmospheric turbulence conditions," *Proc. SPIE* 5895, 58950O (2005).
- [17] Primot, J., Rousset, G., and Fontanella, J. C., "Deconvolution from wave-front sensing: a new technique for compensating turbulence-degraded images," *J. Opt. Soc. Am. A* 7(9), 1598–1608 (1990).
- [18] Fried, D. L., "Least-square fitting a wave-front distortion estimate to an array of phase-difference measurements," *J. Opt. Soc. Am.* 67(3), 370–375 (1977).
- [19] Noll, R. J., "Phase estimates from slope-type wave-front sensors," *J. Opt. Soc. Am.* 68(1), 139–140 (1978).
- [20] Southwell, W. H., "Wave-front estimation from wave-front slope measurements," *J. Opt. Soc. Am.* 70(8), 998–1006 (1980).
- [21] Tyson, R. K., [Principles of Adaptive Optics], 3rd ed., CRC Press, Boca Raton (2011).
- [22] Voitsekhovich, V., Sanchez, L., Orlov, V., and Cuevas, S., "Efficiency of the Hartmann test with different subpupil forms for the measurement of turbulence-induced phase distortions," *Appl. Optics* 40(9), 1299–1304 (2001).
- [23] Herrmann, J., "Least-squares wave front errors of minimum norm," *J. Opt. Soc. Am.* 70(1), 28–35 (1980).
- [24] Wallner, E. P., "Optimal wave-front correction using slope measurements," *J. Opt. Soc. Am.* 73(12), 1771–1776 (1983).
- [25] Roggemann, M. C., "Optical performance of fully and partially compensated adaptive optics systems using least-squares and minimum variance phase reconstructors," *Computers Elect. Eng.* 18(6), 451–466 (1992).
- [26] Bakut, P. A., Kirakosyants, V. E., Loginov, V. A., Solomon, C. J., and Dainty, J. C., "Optimal wavefront reconstruction from a Shack-Hartmann sensor by use of a Bayesian algorithm," *Opt. Comm.* 109, 10–15 (1994).
- [27] Dai, G.-M., "Modified Hartmann-Shack wavefront sensing and iterative wavefront reconstruction," *Proc. SPIE* 2201, 562–573 (1994).
- [28] Roggemann, M. C. and Schulz, T. J., "Algorithm to increase the largest aberration that can be reconstructed from Hartmann sensor measurements," *Appl. Optics* 37(20), 4321–4329 (1998).
- [29] Voitsekhovich, V. V., Bara, S., Rios, S., and Acosta, E., "Minimum-variance phase reconstruction from Hartmann sensors with circular subpupils," *Opt. Comm.* 148, 225–229 (1998).
- [30] Talmi, A. and Ribak, E. N., "Direct demodulation of Hartmann-Shack patterns," *J. Opt. Soc. Am. A* 21(4), 632–639 (2004).
- [31] Talmi, A. and Ribak, E. N., "Wavefront reconstruction from its gradients," *J. Opt. Soc. Am. A* 23(2), 288–297 (2006).
- [32] Canovas, C. and Ribak, E. N., "Comparison of Hartmann analysis methods," *Appl. Optics* 46(10), 1830–1835 (2007).
- [33] Zernike, F., "How I discovered phase contrast," *Science* 121(3141), 345–349 (1955).
- [34] Noll, R. J., "Zernike polynomials and atmospheric turbulence," *J. Opt. Soc. Am.* 66(3), 207–211 (1976).
- [35] Dai, G.-M., "Modal compensation of atmospheric turbulence with the use of Zernike polynomials and Karhunen-Loeve functions," *J. Opt. Soc. Am. A* 12(10), 2182–2193 (1995).
- [36] Mahajan, V. N., "Zernike annular polynomials for imaging systems with annular pupils," *J. Opt. Soc. Am.* 71(1), 75–85 (1981).
- [37] Dai, G.-M., and Mahajan, V. N., "Zernike annular polynomials and atmospheric turbulence," *J. Opt. Soc. Am. A* 24(1), 139–155 (2007).
- [38] Strang, G., [Introduction to Linear Algebra], 4th ed., Wellesley-Cambridge Press, Wellesley (2009).
- [39] Cubalchini, R., "Modal wave-front estimation from phase derivative measurements," *J. Opt. Soc. Am.* 69(7), 972–977 (1979).
- [40] Herrmann, J., "Cross coupling and aliasing in modal wave-front estimation," *J. Opt. Soc. Am.* 71(8), 989–992 (1981).
- [41] Soloviev, O. and Vdovin, G., "Hartmann-Shack test with random masks for modal wavefront reconstruction," *Opt. Express* 13(23), 9570–9584 (2005).
- [42] ten Brummelaar, T. A., "The contribution of high order Zernike modes to wavefront tilt," *Opt. Comm.* 115, 417–424 (1995).
- [43] Fried, D. L., "Optical resolution through a randomly inhomogeneous medium for very long and very short exposures," *J. Opt. Soc. Am.* 56(10), 1372–1379 (1966).
- [44] Fleck, J. A., Morris, J. R., and Feit, M. D., "Time-dependent propagation of high-energy laser beams through the atmosphere," *Appl. Phys.* 10(2), 129–160 (1976).
- [45] Fleck, J. A., Morris, J. R., and Feit, M. D., "Time-dependent propagation of high-energy laser beams through the atmosphere: II," *Appl. Phys.* 14(1), 99–115 (1977).
- [46] Flatte, S. M., Wang, G.-Y., and Martin, J., "Irradiance variance of optical waves through atmospheric turbulence by numerical simulation and comparison with experiment," *J. Opt. Soc. Am. A* 10(11), 2363–2370 (1993).
- [47] Roggemann, M. C. and Welsh, B., [Imaging Through Turbulence], CRC Press, Boca Raton (1996).
- [48] Press, W. H., Teukolsky, S. A., Vetterling, W. T., and Flannery, B. P., [Numerical Recipes: The Art of Scientific Computing], 3rd ed., Cambridge University Press (2007).
- [49] Vorontsov, M. A., Carhart, G. W., Rao Gudimetla, V. S., Weyrauch, T., Stevenson, E., Lachinova, S. L., Beresnev, L. A., Liu, J., Rehder, K., and Riker, J. F., "Characterization of atmospheric turbulence effects over 149 km propagation path using multi-wavelength laser beacons," *Proceedings of the 2010 AMOS Conference*, S. Ryan, ed., The Maui Economic Development Board, Maui, E18 (2010).